Chemical Science

ROYAL SOCIETY OF CHEMISTRY

EDGE ARTICLE

View Article Online
View Journal | View Issue

Cite this: *Chem. Sci.*, 2025, **16**, 22071

All publication charges for this article have been paid for by the Royal Society of Chemistry

Received 24th September 2025
Accepted 15th October 2025

DOI: 10.1039/d5sc07406a

rsc.li/chemical-science

Machine learning-driven prediction of ultrafast spin relaxation in metal halide perovskites for spintronic applications

Jianhui Li,†[a] MingXi Chen,†[b] Pan Wang,†[c] Xiaohong Li,[d] Yuling Huang,[a] Kemi Ding,[d] Lingling Mao,[c] X.-D. Xiang *[e] and Xihan Chen *[a]

Spintronics can reduce the energy consumption of electronic devices. Perovskites have recently emerged as promising spintronic materials. The design of perovskite spintronic devices relies on the understanding and control of spin relaxation processes, which remain challenging. Here, we report a lightweight predictive model for the ultrafast spin relaxation rate based on a set of intrinsic descriptors that are either quantum-chemically computable or directly derivable from molecular composition. The model, constructed using an artificial neural network (ANN) and trained on a curated dataset of 52 perovskite materials (including 14 synthesised and characterised compounds investigated with ultrafast spin dynamics measurements), achieves high predictive accuracy with $R^2 = 0.99$ under leave-one-out cross-validation. SHapley Additive exPlanations (SHAP)-based interpretability analysis further reveals clear physical correlations between the spin relaxation rate and frontier orbital energies (HOMO and LUMO), molecular weight, polarizability, and dipole moment, clarifying how modulation of spin–orbit coupling, phonon scattering, and electron–hole exchange pathways act as primary mechanisms governing spin decoherence. This work establishes a generalizable and physically interpretable pre-synthetic design strategy for the rational development of spin-functional perovskite materials.

Introduction

Spintronics, which leverages the intrinsic spin of electrons as an information carrier, has emerged as a promising paradigm in next-generation electronics.[1–5] Owing to its advantages in power efficiency, operation speed, and device integration, spintronics holds great potential for applications in quantum computing, information storage, spin valves, and optoelectronic systems.[2,6–8] Among the key parameters governing device performance, the spin relaxation lifetime plays a crucial role in determining spin transport behaviour and overall device efficiency.[6,9,10] Metal halide perovskites (general formula ABX_3, where A is an organic cation or Cs, B = Pb^{2+} or Sn^{2+} and X = Cl, Br, or I) have rapidly emerged as promising candidates for spintronic research owing to their exceptional optoelectronic properties, including long carrier diffusion lengths, tunable bandgaps, and strong spin–orbit coupling (SOC).[11,12] These materials have also demonstrated outstanding performance in a wide range of optoelectronic devices, such as photovoltaics, light-emitting diodes, photodetectors, and spin-valve systems.[13–16]

Despite the tremendous potential of perovskite materials, accurately predicting their spin dynamics remains a significant challenge. This difficulty stems from two aspects. Primarily, spin relaxation involves multiple intertwined microscopic mechanisms,[17] with different pathways competing under varying material systems and excitation conditions, leading to pronounced material sensitivity and physical complexity. At the physical mechanism level, SOC serves as a fundamental factor governing spin dynamics in perovskites, especially in two-dimensional systems containing heavy elements such as Pb and I, where strong SOC induces pronounced Rashba splitting and alters the spin polarization states.[18,19] In the absence of inversion symmetry, the D'yakonov–Perel' (DP) mechanism typically dominates spin decoherence behaviour.[20,21] Under this mechanism, electrons precess around a momentum-dependent intrinsic magnetic field $\vec{\Omega}(\varepsilon)$, and each momentum scattering event randomises the precession direction, thereby leading to

[a]State Key Laboratory of Quantum Functional Materials, SUSTech Energy Institute for Carbon Neutrality, Department of Mechanical and Energy Engineering, Southern University of Science and Technology, Shenzhen, Guangdong, 518055, China. E-mail: chenxh@sustech.edu.cn

[b]Department of Material Science and Engineering, Southern University of Science and Technology, Shenzhen, Guangdong, 518055, China

[c]Department of Chemistry, Southern University of Science and Technology, Shenzhen, Guangdong, 518055, China

[d]School of Automation and Intelligent Manufacturing, Southern University of Science and Technology, Shenzhen, Guangdong, 518055, China

[e]Songshan Lake Materials Laboratory, Dongguan, Guangdong 523808, China. E-mail: xdxiang@iphy.ac.cn

† These authors contributed equally to this work.

the loss of spin information. The corresponding spin relaxation rate is given by the following expression:[17,22]

$$\tau_{DP}^{-1} = \frac{2}{3}\frac{\int_0^\infty d\varepsilon\rho(\varepsilon)\overline{\Omega^2}\tau_p(\varepsilon)[F_+(\varepsilon) - F_-(\varepsilon)]}{\int_0^\infty d\varepsilon\rho(\varepsilon)[F_+(\varepsilon) - F_-(\varepsilon)]} \quad (1)$$

where $\rho(\varepsilon)$ is the density of states, $\tau_p(\varepsilon)$ is the momentum relaxation time, $F_\pm(\varepsilon)$ are the Fermi distribution functions for spin-up and spin-down states, and $\overline{\Omega^2}(\varepsilon)$ represents the averaged square of the spin precession frequency. In addition to the D'yakonov–Perel' (DP) mechanism, when impurity or phonon scattering is present, the Elliott–Yafet (EY) mechanism becomes significant. In this case, spin relaxation originates from spin-mixed Bloch states that undergo momentum scattering. The spin relaxation rate can be expressed as:[17,23]

$$\tau_{EY}^{-1} = 8\pi T\int_0^\infty d\Omega\alpha_s^2F(\Omega)\frac{\partial N(\Omega)}{\partial T} \approx \langle b^2\rangle/\tau_p \quad (2)$$

where $\alpha_s^2F(\Omega)$ is the spin-flip Eliashberg function, $N(\Omega)$ is the Bose–Einstein distribution function, and Ω denotes the phonon frequency. The expression can be simplified with $\langle b^2\rangle/\tau_p$, where $\langle b^2\rangle$ is the average squared spin-flip matrix element, and τ_p is the momentum relaxation time. Under high carrier excitation conditions, the Bir–Aronov–Pikus (BAP) mechanism becomes significant, accelerating spin relaxation through electron–hole exchange interactions. The complete expression for the spin relaxation rate is:[17]

$$\tau_{BAP}^{-1} = \frac{2}{\tau_0}N_a\alpha_B^3\frac{V_k}{V_B}\left[\frac{P}{N_a}|\psi(0)|^4 + \frac{5}{3}\frac{N_a - p}{N_a}\right] \quad (3)$$

where $\tau_0 = \hbar/\Delta_{ex}$ is the characteristic timescale related to the excitonic exchange energy Δ_{ex}; α_B is the exciton Bohr radius; V_k and $V_B = \hbar/(m_c\alpha_B)$ denote the electron and Bohr velocities, respectively; p is the hole concentration; N_a is the density of states at the valence band maximum; and $|\psi(0)|^2$ is the electron–hole overlap probability at zero separation. This differentiation highlights the strong sensitivity of spin relaxation to carrier density and statistical behavior. In addition to these mechanisms, recent studies have revealed that polaron formation and the impact of structural chirality in perovskites can also affect spin dynamics.[22–26] All these phenomena suggest that spin relaxation is not solely governed by scattering processes but is also intimately related to electron–lattice interactions.

In contrast, spin relaxation typically occurs on ultrafast timescales—from picoseconds to sub-picoseconds—placing stringent demands on experimental time resolution. Current characterization techniques primarily rely on ultrafast pump–probe optical methods, such as time-resolved magneto-optical Kerr effect (TR-MOKE), TR-Faraday rotation, and transient spin grating (TSG) spectroscopy.[27–29] While these techniques offer excellent temporal resolution, the measurement process remains complex, time-consuming, and inherently low-throughput, posing a significant bottleneck for rapid performance evaluation and high-throughput screening of spin-functional perovskite materials. Previous studies, such as those by Chen *et al.*, have reported a quadratic relationship between the spin relaxation rate and the exciton binding energy (E_b),[20,22] providing a valuable reference for future lifetime prediction and material optimization. However, estimating E_b in lead halide perovskites remains highly controversial, with substantial discrepancies arising across different experimental techniques. For example, reported E_b values for $MAPbI_3$ range widely from 9 to over 100 meV depending on the measurement method.[30,31] These inconsistencies cast doubt on the reliability of E_b as a standalone predictor, highlighting the need for a more accurate and efficient predictive framework to guide material design.

In recent years, machine learning has been widely adopted in materials science due to its data-driven efficiency and predictive capabilities.[32–37] ML has found successful applications across various domains, including organic synthesis,[32,38] materials property prediction,[39,40] and process optimization.[35,41] In the context of perovskite research, ML has also demonstrated substantial potential, being employed to predict bandgaps and optical properties, unravel stability mechanisms, and guide crystallisation processes,[42–44] thereby supporting the development of high-performance optoelectronic devices. For instance, Wu *et al.* developed a closed-loop system that integrates machine learning with high-throughput organic synthesis,[42] enabling the inverse design of hole-transport materials for perovskite solar cells based on molecular descriptors. This strategy led to the discovery of a high-efficiency molecule with a power conversion efficiency of up to 26.2%, showcasing the powerful role of ML in functional material discovery and design. Despite its importance, the spin relaxation lifetime in perovskite materials has remained largely unaddressed by machine learning, and a systematic modelling framework has yet to be established.

To address the challenge of predicting ultrafast spin lifetimes in perovskites, we developed a small-sample machine learning strategy guided by experimental validation. We initially constructed a hybrid model incorporating both structure-dependent descriptors—such as exciton binding energy and interlayer spacing—and intrinsic features derived from quantum chemical calculations. This model achieved excellent predictive performance ($R^2 = 0.98$), underscoring the importance of structural parameters in governing spin behaviour. However, the reliance on post-synthetic structural measurements limited its applicability in early-stage material screening. To improve generalizability and enable pre-synthetic evaluation, we refined the descriptor set by removing all experimentally derived inputs and retaining only those features that are either quantum-chemically computable or directly derivable from molecular composition. The resulting lightweight model was trained on an expanded dataset of 52 perovskite samples, including 14 synthesized and ultrafast-characterized compounds. To rigorously assess predictive performance, we first trained the model on a subset of 45 samples and tested it on the remaining 7 unseen compounds. This split-sample strategy yielded high predictive accuracy ($R^2 = 0.95$), confirming the model's ability to generalize to new materials. We then employed leave-one-out cross-validation (LOOCV) on the full dataset of 52 samples to maximize the predictive potential of the descriptor set and perform interpretability analysis. The

final model achieved an R^2 of 0.99, demonstrating strong robustness across diverse compositions. Additionally, to avoid confusion with 'multivariate linear fitting,' we evaluated a MLR baseline using the same eight intrinsic descriptors and the 38/14 train–test split; its independent test-set $R^2 = 0.34$, markedly below the ANN's $R^2 = 0.76$, further evidencing significant nonlinearity and inter-feature coupling in spin-relaxation prediction. SHAP analysis identified molecular weight, HOMO energy, and LUMO energy as the most influential features, revealing their direct roles in modulating spin–orbit coupling, phonon scattering, and electron–hole exchange interactions. Polarizability and dipole moment were also found to contribute meaningfully to spin relaxation dynamics. Overall, this work establishes a lightweight, interpretable, and computation-accessible prediction framework for pre-synthetic screening, offering practical tools and mechanistic insight for the rational design of spin-functional perovskite materials.

Machine learning framework for spin relaxation prediction

To enable pre-synthetic prediction of the spin relaxation rate in perovskite materials, we developed a lightweight machine learning model based on a small but well-curated dataset. As illustrated in Fig. 1, the workflow comprises four core modules: dataset construction, descriptor generation and selection, model training and validation, and model interpretation and mechanistic analysis.

A dataset comprising 52 halide-perovskite single crystral materials with experimentally measured spin relaxation rates was assembled, including 38 entries collected from the published literature[20,22,23,45–60] and 14 samples synthesized and characterized in this study based on reported procedures. These additional samples were introduced to enrich the training set and enhance the model's generalizability. The literature-derived samples were annotated with both structural descriptors and intrinsic physical descriptors (see Tables S1 and S2 of the SI), while the synthesized materials and their corresponding descriptors are summarized in Table S3. Here, the spin relaxation rate used for modelling is defined as the inverse of the extracted spin lifetime ($\tau_{1/2}{}^{-1}$).

Given that spin behaviour is influenced by both structural and electronic factors, two feature input pathways were designed: Path A integrates structure-related descriptors—including exciton binding energy, Pb–I distance, lattice volume, spacing of layer, and average lattice angle—with intrinsic

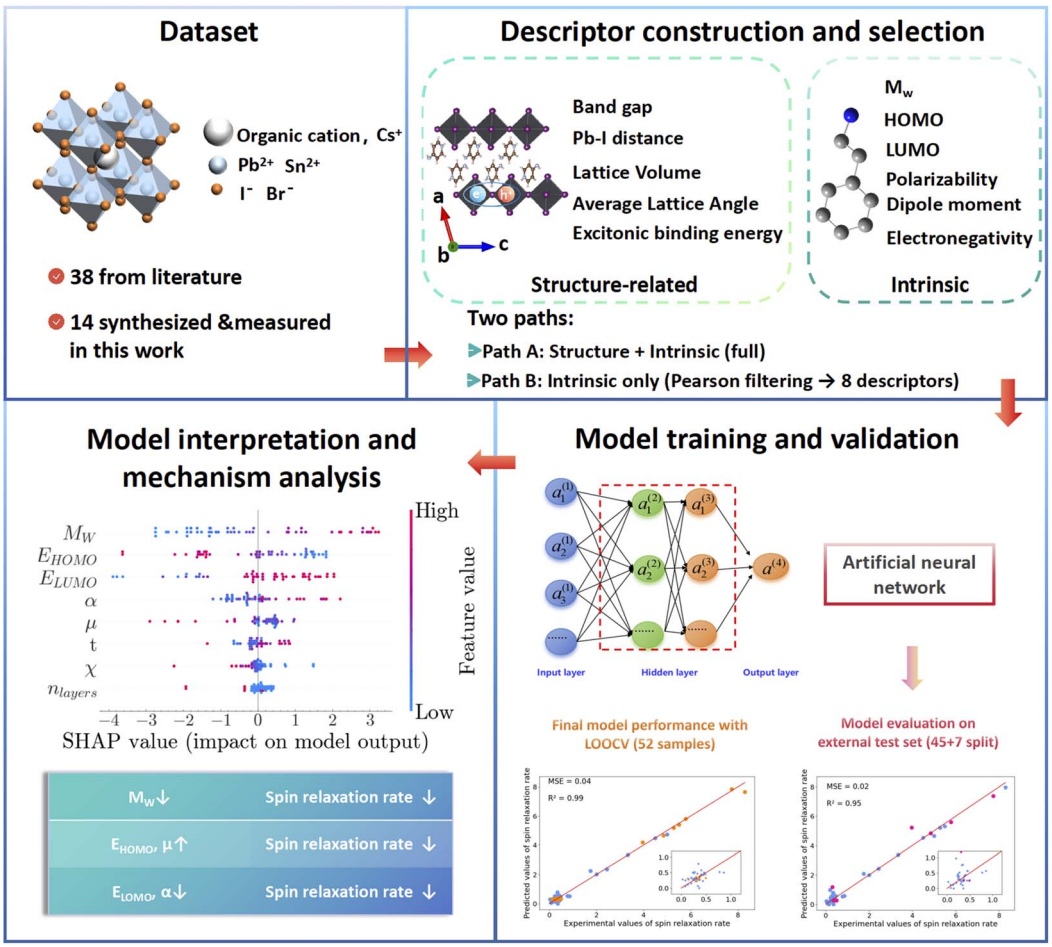

Fig. 1 Overall workflow of this study for the machine learning-based prediction of spin relaxation rate in perovskite materials.

physical properties. Path B includes only intrinsic descriptors that are either obtained from quantum chemical calculations (*e.g.*, polarizability, dipole moment, and HOMO/LUMO energy levels) or directly derived from molecular composition (*e.g.*, molecular weight), totalling 10 descriptors. Pearson correlation analysis (with a threshold of $|r| > 0.9$) was applied to eliminate highly collinear features, yielding a final set of 8 descriptors for model training. The complete list of descriptors, along with definitions and values, is provided in Tables S1–S3. For detailed procedures for calculating each descriptor, see the SI.

To build the predictive model, an artificial neural network (ANN) was employed and trained using a leave-one-out cross-validation (LOOCV) strategy. During model selection, we benchmarked several widely used machine learning algorithms, including random forest (RF), support vector regression (SVR), and extreme gradient boosting (XGBoost). Among these, the ANN demonstrated superior predictive performance and robustness across multiple subsets and was therefore chosen as the core model for subsequent analysis. To rigorously assess the model's generalization capability, we first trained the ANN on a subset of 45 samples (38 literature-reported and 7 synthesized) and evaluated its performance on 7 unseen synthesized compounds, achieving an R^2 of 0.95. Following this validation, we retrained the model on the full set of 52 samples using LOOCV to maximize predictive performance and model interpretability. The final lightweight model, constructed using eight intrinsic descriptors from Path B, achieved an R^2 of 0.99 and an MSE of 0.04. Detailed evaluation metrics are provided in the SI.

To interpret the contribution of each descriptor to the predicted spin relaxation rates, SHapley Additive exPlanations (SHAP) analysis was performed on the final ANN model trained *via* LOOCV. SHAP values were used to quantify both the importance and directional impact of each intrinsic descriptor on the model output. Further mechanistic analysis was carried

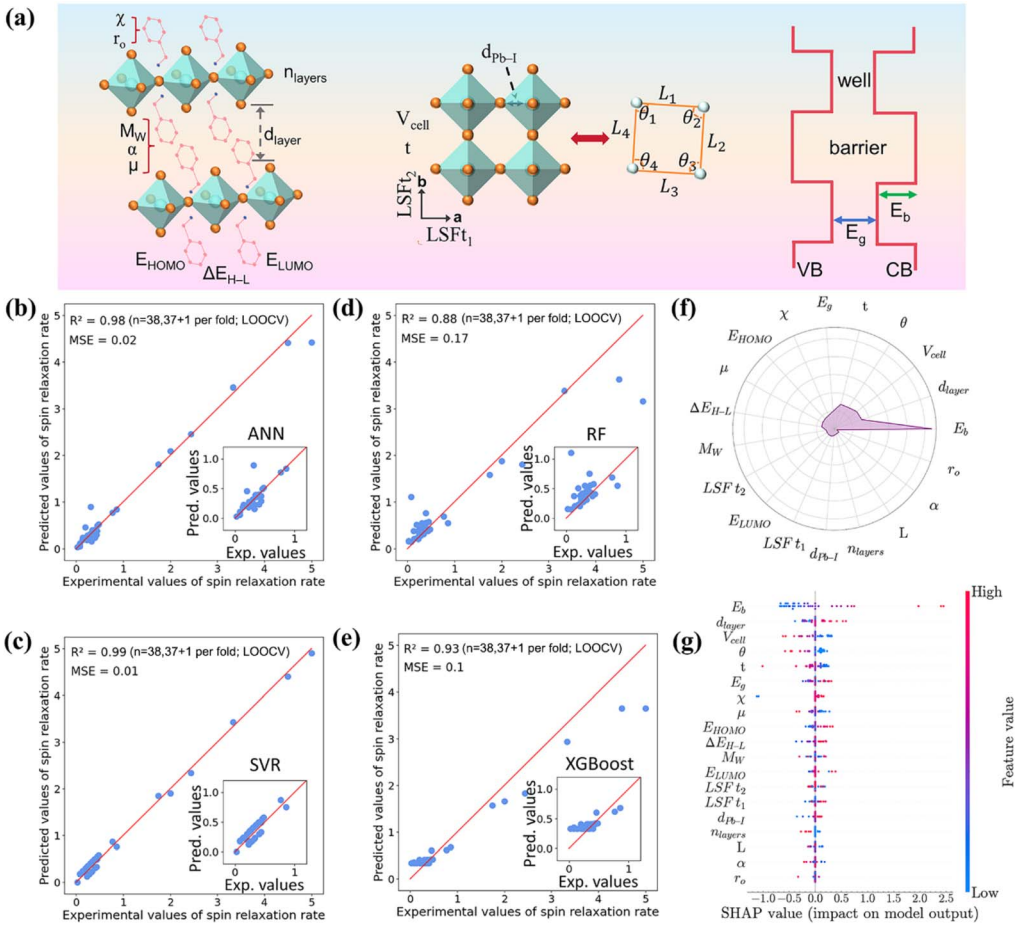

Fig. 2 (a) Schematic illustration of structural and intrinsic descriptors used in the predictive model, including electronegativity (χ), organic molecular radius (r_o), number of layers (n_{layers}), molecular weight (M_W), polarizability (α), dipole moment (μ), spacing of layers (d_{layer}), HOMO energy (E_{HOMO}), LUMO energy (E_{LUMO}), HOMO–LUMO gap (ΔE_{H-L}), Pb–I bond distance (d_{Pb-I}), lattice volume (V_{cell}), tolerance factor (t), layer shift factors (LSF t_1 and LSF t_2), lattice parameters (L), lattice angle (θ), excitonic binding energy (E_b), and band gap (E_g). (b–e) Predicted *versus* experimental spin-relaxation rates for the 38 literature-reported perovskite samples using (b) ANN, (c) SVR, (d) RF, and (e) XGBoost. All R^2 values in panels (b–e) are computed by leave-one-out cross-validation (LOOCV) on the 38-sample literature set. The red diagonal indicates $y = x$. (f) Radar chart showing the relative importance of each descriptor as calculated from the ANN-based SHAP analysis. (g) SHAP summary plot illustrating the magnitude and direction of each feature's contribution to the predicted spin relaxation rate. Positive SHAP values correspond to increasing spin relaxation rate.

out based on the physical meaning of the leading descriptors identified through SHAP.

Results and discussion

To construct a predictive model for the spin relaxation rate of perovskite materials, we first established a comprehensive descriptor system that integrates both structural and intrinsic molecular features, as schematically illustrated in Fig. 2a. Structural descriptors include the spacing of layers (d_{layer}), lattice volume (V_{cell}), excitonic binding energy (E_b), band gap (E_g), average lattice parameters (L), average lattice angle (θ), number of layers (n_{layers}), tolerance factor (t), Pb–I bond distance (d_{Pb-I}), and layer shift factors (LSFt_1 and LSFt_2), and intrinsic physical attributes that are computable *via* quantum chemistry include polarizability (α), dipole moment (μ), electronegativity (χ), average molecular weight (M_W), organic molecular radius (r_o), HOMO energy (E_{HOMO}), LUMO energy (E_{LUMO}), and the HOMO–LUMO gap (ΔE_{H-L}). These descriptors are designed to capture the key structural factors and electronic properties governing spin relaxation processes. We then systematically evaluated four widely used regression algorithms using 38 literature-reported samples: ANN, SVR, RF, and XGBoost. As shown in Fig. 2b–e, all models exhibited strong predictive performance on this dataset. Among them, SVR achieved the highest predictive accuracy ($R^2 = 0.99$, MSE = 0.01), followed by ANN ($R^2 = 0.98$, MSE = 0.02) and XGBoost ($R^2 = 0.93$, MSE = 0.17), while RF performed comparatively worse ($R^2 = 0.88$, MSE = 0.17). These results indicate that, even under small-sample conditions, machine learning models can achieve reliable predictions of spin relaxation behaviour when trained on a carefully constructed set of descriptors.

Although the SVR model achieved the highest R^2 in the initial benchmarking, we ultimately selected the ANN model as the basis for SHAP analysis, based on the following considerations: (1) ANN exhibits strong nonlinear fitting capability, making it well-suited to model complex relationships between spin relaxation and intrinsic physical properties; (2) although the SHAP framework is generally model-agnostic, the continuous and differentiable architecture of ANN is particularly compatible with deep-learning-based SHAP variants (*e.g.*, Deep SHAP), enabling more efficient and physically intuitive interpretation of feature contributions; and (3) ANN demonstrates strong adaptability to small-sample datasets, maintaining high predictive reliability even under limited data conditions.[61,62] Based on this, we employed the ANN model for SHAP-based interpretability analysis and visualized the feature contributions and directional impacts using a radar chart (Fig. 2f) and a SHAP summary plot (Fig. 2g). All subsequent model refinements, retraining steps, and interpretability analyses were consistently based on the ANN framework.

Among all features, the exciton binding energy exhibits the most significant influence on the model output, with the widest SHAP distribution and the highest mean contribution, indicating that E_b is the dominant descriptor for predicting the spin-relaxation rate. The model reveals a clear positive correlation: higher exciton binding energies (red points) are associated with higher predicted spin relaxation rates, corresponding to shorter spin lifetimes. This trend is highly consistent with prior experimental observations.[20,22] Chen *et al.* reported a quadratic relationship between exciton binding energy and the spin relaxation rate in two-dimensional perovskites,[20] where stronger excitonic confinement (larger E_b) enhances exchange interactions and thus accelerates spin decoherence, resulting in shorter spin lifetimes. These results further reaffirm the role of E_b as a key governing factor for spin relaxation dynamics in halide perovskites.

In addition, structural descriptors such as layer spacing, lattice volume, and average lattice angle also exhibit notable importance in the SHAP analysis. We propose that the influence of these structural parameters on spin relaxation behaviour largely stems from their regulation of excitonic binding characteristics. Specifically, an increase in layer spacing typically weakens quantum confinement and dielectric screening effects, leading to a reduction in exciton binding energy. This diminishes the spin protection effect and accelerates spin decoherence. This observation is consistent with experimental findings in two-dimensional Ruddlesden–Popper perovskites,[45] where structures with lower quantum well order (*i.e.*, larger interlayer spacing) typically show faster spin relaxation. Lattice volume and average lattice angle also exhibit notable influence. Smaller lattice volumes and more distorted bond angles (*i.e.*, lower average lattice angles) are generally associated with higher spin relaxation rates. This suggests that compressed or distorted lattice environments may enhance local spin–orbit coupling perturbations or phonon–spin interactions, thereby accelerating spin decoherence through the DP or EY mechanisms.

Moreover, although the dipole moment and HOMO/LUMO energy levels exhibit relatively lower mean SHAP contributions, they still show consistent directional trends across samples. These features may influence spin relaxation indirectly through their modulation of orbital symmetry, electron localization, or energy level alignment, indicating the existence of non-dominant but physically relevant pathways for spin regulation.

The SHAP analysis described above revealed a strong dependence of the model on several structural descriptors—such as exciton binding energy, interlayer spacing, and lattice volume. While this outcome is not unexpected, it reinforces existing literature findings that these structural parameters are closely correlated with spin relaxation behaviour in halide perovskites. However, to improve the model's practical utility and generalizability, we further refined the feature selection strategy. Given that structure-related parameters typically require post-synthetic experimental measurements—which are time-consuming and unsuitable for early-stage material design or high-throughput screening—we removed all descriptors that depend on experimental inputs. Instead, we retained only two categories of features: (i) quantum-chemically derived descriptors, including dipole moment, polarizability, HOMO and LUMO energy levels, HOMO–LUMO gap, and the molecular radius of the organic cation; and (ii) composition- or structure-derived descriptors based on chemical formulae or empirical rules, such as electronegativity, molecular weight, tolerance

factor, and the number of inorganic layers in the perovskite framework. The selection of these descriptors was primarily motivated by the need to ensure that they not only capture the key physical mechanisms governing spin relaxation in perovskite materials but are also computable or derivable without requiring any experimental data, thereby enabling their use in early-stage material design and high-throughput screening.

Specifically, the HOMO and LUMO energy levels, as well as the HOMO–LUMO gap (ΔE_{H-L}), describe the distribution of frontier molecular orbitals, which are closely related to band alignment, electron–hole wavefunction overlap, and exciton binding behavior. The dipole moment (μ) and polarizability (α) characterize the electrostatic and electronic properties of the organic cation, influencing local electric fields, interface energetics, and phonon perturbations. The molecular radius of the organic cation (r_o) and electronegativity (χ) reflect the spatial size and bonding characteristics of the organic molecules, determining their impact on crystal symmetry, dielectric screening, and carrier localization. Molecular weight (M_w) partially reflects the molecular volume and structural complexity, which are related to lattice packing and dielectric environment. Finally, the tolerance factor (t) and the number of inorganic layers (n_{layers}) provide geometric and structural constraints, describing crystal framework stability and quantum confinement effects, both of which play an essential role in spin relaxation. Importantly, these 10 descriptors are either fully computable using quantum chemical calculations or directly derivable from chemical composition, thus making them highly suitable for pre-synthetic material screening and predictive modelling without relying on any post-synthesis experimental measurements.

To reduce redundancy and avoid multicollinearity, Pearson correlation analysis was performed (Fig. 3a). The Pearson correlation coefficient r between two variables x and y is calculated as:[63]

$$r = \frac{\sum_{i-1}^{n}(x_i - \bar{x})(y_i - \bar{y})}{\sqrt{\sum_{i=1}^{n}(x_i - \bar{x})^2}\sqrt{\sum_{i-1}^{n}(y_i - \bar{y})^2}} \quad (4)$$

where x_i and y_i are the values of the two descriptors for the ith sample, and $\bar{x}$ and $\bar{y}$ denote their respective means. Using a correlation threshold of $|r| > 0.9$ and guided by physical intuition, we ultimately excluded two redundant features—organic molecular radius and HOMO–LUMO gap—retaining the remaining 8 descriptors for model training. The full list of retained and excluded descriptors is summarized in Table S4 (SI).

Based on this refined feature set, we then retrained the ANN model using the original 38 literature-reported samples and evaluated its performance using LOOCV. As shown in Fig. 3b, the ANN model achieved high predictive accuracy ($R^2 = 0.94$, and an MSE = 0.08) without using any structure-based features, indicating that these intrinsic, fully computable descriptors contain sufficient physical information to effectively model spin relaxation dynamics. Although LOOCV on the 38 literature-reported samples demonstrates that the ANN model achieves high predictive accuracy ($R^2 = 0.94$), this validation strategy primarily assesses the model's fit to known data and offers limited insight into its generalization performance on previously unseen materials.

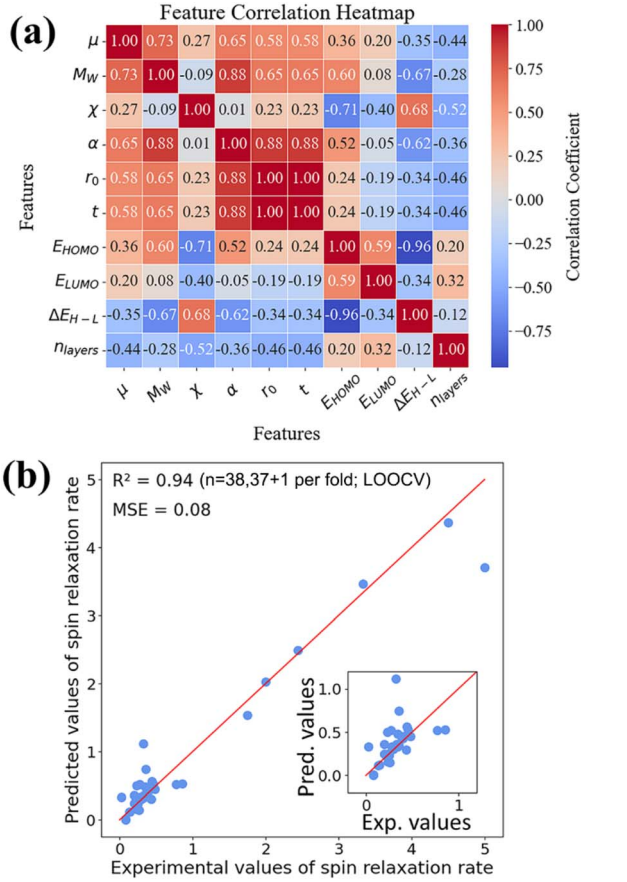

Fig. 3 (a) Pearson correlation heatmap of ten intrinsic and computationally accessible descriptors initially selected for lightweight modelling. (b) Predicted *versus* experimental spin-relaxation rates using the ANN model trained on the reduced set of eight intrinsic descriptors and 38 literature-derived samples. The R^2 reported in this panel is obtained *via* LOOCV on the 38-sample set. The inset highlights the low-rate regime.

To further evaluate the model's predictive capability for unknown systems, we synthesized 14 two-dimensional Pb based perovskite materials and experimentally measured their spin relaxation lifetimes using ultrafast spectroscopy. The selection of these samples was based on the following considerations. First, we aimed to cover a broad structural diversity within a limited sample size. The 14 compounds include different structural families, such as Ruddlesden–Popper (RP) and Dion–Jacobson (DJ) phases, as well as various quantum well thicknesses ($n = 1, 2, 3$), allowing us to systematically examine the influence of layer number, quantum confinement, and lattice symmetry on spin relaxation behaviour. Second, in choosing the organic cations, we deliberately introduced diverse chemical functionalities and molecular types, including aromatic derivatives (F-PMA, Br-PMA, I-PMA, and *p*-MePEA), flexible

alkylamines (*n*BA and iBA), rigid cyclic molecules (CMA and APD), and functional groups with strong polarity (3AMPY, 4AMPY, and ThMA). These variations provide a wide range of dielectric environments, symmetry breaking, and Rashba field strengths, enabling us to comprehensively explore the molecular-level effects on spin relaxation mechanisms. Finally, experimental feasibility and data consistency were also considered. All compounds can be synthesized under consistent conditions using well-established hot-solution growth methods, ensuring the reliability and comparability of the measured spin lifetimes. Additionally, XRD and UV-vis characterization studies were performed on these synthesized samples, and the corresponding results are provided in Fig. S1 and S2 of the SI. Fig. 4 illustrates the workflow for spin relaxation dynamics measurements in 2D perovskite materials and presents representative experimental results. The transient reflectance spectra for other materials are provided in Fig. S3 of the SI. In two-dimensional halide perovskites, including both RP and DJ phases, the band-edge states primarily consist of s-like valence bands derived from hybridized Pb 6s and I 5p orbitals, along with conduction band split states formed by strong spin–orbit coupling (SOC) induced splitting of Pb 6p orbitals.[22] As depicted in Fig. 4a, according to spin-dependent optical transition selection rules, excitons in the ground state can be selectively excited using circularly polarized pump pulses: right-handed (σ^+) polarization generates excitons with angular momentum projection $|+1\rangle$, while left-handed (σ^-) polarization generates $|-1\rangle$ excitons.[20,22,23]

In spin-resolved transient reflection (TR) measurements, the probe polarization is fixed to σ^+, while the pump polarization is varied between co-circular ($\sigma^+\sigma^+$, SC configuration) and counter-circular ($\sigma^-\sigma^+$, CC configuration) modes. In the SC configuration, the σ^+ probe monitors the decay of $|+1\rangle$ excitons, whereas in the CC configuration, it detects the formation of $|+1\rangle$ excitons. By comparing transient reflection changes between SC and CC modes, the spin relaxation dynamics of the exciton populations can be effectively extracted.

Fig. 4b shows the structures of the 11 organic cations employed to synthesize the 14 perovskite samples investigated. Some organic cations were used to construct multiple layer thicknesses (*n* values) of 2D perovskite structures, such as nBA for $n = 2$ and 3, and 4AMPY for $n = 2$ and 3. To illustrate typical spin behaviour across different structural systems, two representative materials were selected for detailed analysis: (APD)PbI_4, which exhibits a relatively long spin lifetime, and $(ThMA)_2PbI_4$, characterized by ultrafast spin relaxation. Fig. 4c and f present the 2D transient reflection pseudocolor maps under SC and CC configurations for (APD)PbI_4 and $(ThMA)_2PbI_4$, respectively, while Fig. 4d and g show the transient reflection spectra at a 0.3 ps delay for these two materials. In

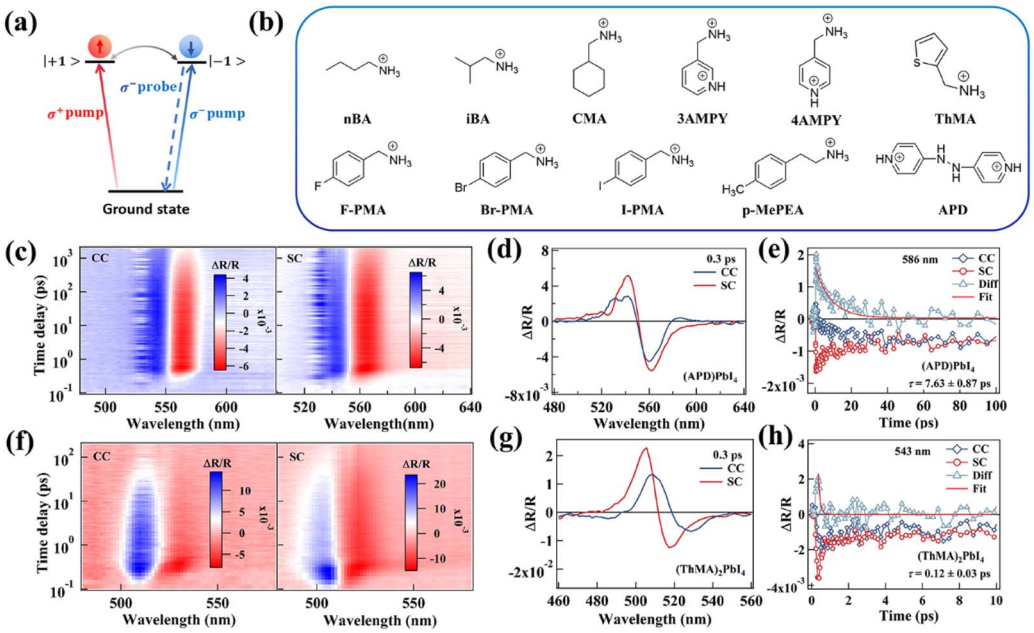

Fig. 4 (a) Schematic diagram of the spin-resolved transient reflection (TR) measurement setup. (b) Molecular structures of ten organic cations used to synthesize fourteen 2D halide perovskite samples, including both Dion–Jacobson and Ruddlesden–Popper phases. The cations are *n*-butylammonium (*n*BA), iso-butylammonium (iBA), cyclohexylmethylammonium (CMA), 3-aminopyridinium (3AMPY), 4-aminopyridinium (4AMPY), thiomethylammonium (ThMA), 4-fluorophenylmethylammonium (F-PMA), 4-bromophenylmethylammonium (Br-PMA), 4-iodophenylmethylammonium (I-PMA), *p*-methylphenethylammonium (*p*-MePEA), and 1,2-di(pyridin-4-yl)diazene (APD). (c) Pseudocolor maps of transient reflection spectra for (APD)PbI_4 under CC (left) and SC (right) configurations. (d) Transient reflection spectra of (APD)PbI_4 at 0.3 ps delay under SC and CC configurations, measured with a pump wavelength of 550 nm and a fluence of 3.48 μJ cm^{-2}. (e) Spin relaxation kinetics of (APD)PbI_4 obtained by differential reflection signal ΔR(SC) − ΔR(CC). (f) Pseudocolor maps of transient reflection spectra for $(ThMA)_2PbI_4$ under CC (left) and SC (right) configurations. (g) Transient reflection spectra of $(ThMA)_2PbI_4$ at 0.3 ps delay under SC and CC configurations, measured with a pump wavelength of 515 nm and a fluence of 3.87 μJ cm^{-2}. (h) Spin relaxation kinetics of $(ThMA)_2PbI_4$ obtained by differential reflection signal ΔR(SC) − ΔR(CC).

both cases, pronounced photobleaching (PB) features are observed in the excitonic absorption region, attributed to phase-space filling effects resulting from exciton formation. For (APD)PbI_4, the excitonic absorption peak appears around 560 nm ($E_g \approx 2.19$ eV), with a distinct photoinduced absorption (PA) feature emerging near 570 nm, indicating the partial preservation of spin polarization on an ultrafast timescale. In contrast, for $(ThMA)_2PbI_4$, although a PB feature is observed near 515 nm ($E_g \approx 2.41$ eV), no clear PA signal is detected, suggesting rapid spin depolarization in this material. Fig. 4e and h further show the evolution of the differential reflection signals (ΔR(SC) − ΔR(CC)) over time for (APD)PbI_4 and $(ThMA)_2PbI_4$, respectively. Single-exponential fitting yields spin relaxation times ($\tau_{1/2}$) of approximately 7.76 ± 0.84 ps for (APD)PbI_4 and 0.12 ± 0.03 ps for $(ThMA)_2PbI_4$. These results highlight the critical influence of organic cation electronic structures and molecular conformations on exciton spin retention, providing an experimental basis for exploring the intrinsic structure–spin property correlations. Additional transient reflectance dynamics of other synthesized materials are provided in Fig. S4 of the SI.

Given that the spin relaxation rates reported in the literature are predominantly concentrated in the lower range, we sought to mitigate the skewed distribution of the training set by incorporating seven representative compounds selected from the 14 synthesized perovskites prepared in this work. This selection strategy was designed to broaden the coverage of response space, enhance training diversity, and improve the model's ability to learn across a wider range of spin relaxation behaviours. In addition, given the potential differences in experimental instrumentation and measurement protocols between literature data and our own measurements, partially integrating the synthesized samples into the training process helped reduce systematic bias and improve the model's adaptability and generalization under practical experimental conditions. Table S5 summarizes the allocation of literature-reported and synthesized samples into the training and external test sets for model development and evaluation.

As a result, we constructed a training set comprising 45 samples (38 literature-reported and 7 synthesized in this work) and used the remaining 7 synthesized compounds as an external test set to evaluate the model's real-world predictive performance. As shown in Fig. 5a, the ANN model trained on this dataset exhibited good predictive accuracy on the 7 independent test samples, with predicted values generally showing strong linear correlation with the experimental results. After 800 training iterations (optimization details are provided in Fig. S5), the model achieved an R^2 of 0.95, demonstrating the strong generalizability and reliability of the selected intrinsic descriptor set and ANN framework in predicting spin relaxation behavior in previously untested perovskite materials. In addition, certain individual samples exhibited noticeable deviations between experimental and predicted spin relaxation rates, particularly for those with relatively small relaxation rates, such as $(n\text{BA})_2(\text{MA})Pb_2I_7$ and $(\text{4AMPY})_2(\text{MA})Pb_3I_{10}$. These deviations were primarily attributed to the inherent prediction fluctuations commonly encountered when small-sample machine learning models are extrapolated to previously unseen compounds. Notably, despite differences in organic cation types and structural parameters among the test samples, the model consistently maintained strong linearity and stability across a broad response range, demonstrating the robust adaptability and generalizability of the intrinsic descriptor framework and ANN model in predicting spin relaxation behaviour across diverse two-dimensional perovskite systems. Table S6 lists the experimental and predicted spin relaxation rates for the 7 synthesized perovskite samples used as the external test set. To more stringently evaluate extrapolation, we conducted a fully independent test using 38 literature samples for training and 14 synthesized samples for testing (Fig. S6). The model trained solely on literature data and the selected intrinsic descriptors achieves a test set $R^2 = 0.76$ on these previously unseen samples, indicating robust extrapolation across chemical/structural diversity even with limited overall data. In addition, we constructed a learning curve (test-set R^2 *versus* training-set size; see Fig. S6), which shows a steady improvement in predictive performance as the number of training samples increases, corroborating the model's stability and scalability across different data-regime sizes.

To rule out the possibility that a multivariate linear fit could achieve comparable performance, we explicitly examined a multilinear regression (MLR) baseline. MLR assumes a linear additive relation between the target y (spin-relaxation rate) and descriptors x_i:

$$y = \beta_0 + \sum_{i-1}^{n} \beta_i x_i + \varepsilon \quad (5)$$

Coefficients β_i were estimated by ordinary least squares (OLS). Using the same eight intrinsic descriptors, identical standardization, and the same train/test split (38 literature samples for training; 14 synthesized, completely unseen samples for testing), we estimated coefficients by ordinary least squares (OLS). To avoid artificially weakening the linear baseline due to multicollinearity, we applied the same Pearson correlation screen with a threshold of $|r| > 0.9$ used elsewhere. Under these controlled conditions, the MLR attains a test-set $R^2 = 0.34$ (Fig. S7), which is far below the ANN's $R^2 = 0.76$ on the identical split. Given that dominant spin-relaxation pathways (DP/EY/BAP) involve pronounced nonlinearity and inter-feature interactions—for example, DP is jointly modulated by Rashba field strength and momentum-scattering time; EY depends multiplicatively on $\langle b^2 \rangle$ and τ_p; and BAP is nonlinearly sensitive to electron–hole wavefunction overlap/exchange—an additive linear model cannot capture this physics. The ANN's superior extrapolation therefore stems from its capacity to represent such nonlinear and higher-order couplings.

Building on this foundation, we incorporated all 52 samples into the model construction to maximize its expressive capacity and predictive robustness. The final model was trained using LOOCV to ensure reliable and interpretable predictions. As shown in Fig. 5b, the ANN model exhibited strong linear correlation between predicted and experimental spin relaxation rates across the full dataset, achieving an R^2 of 0.99 and an MSE

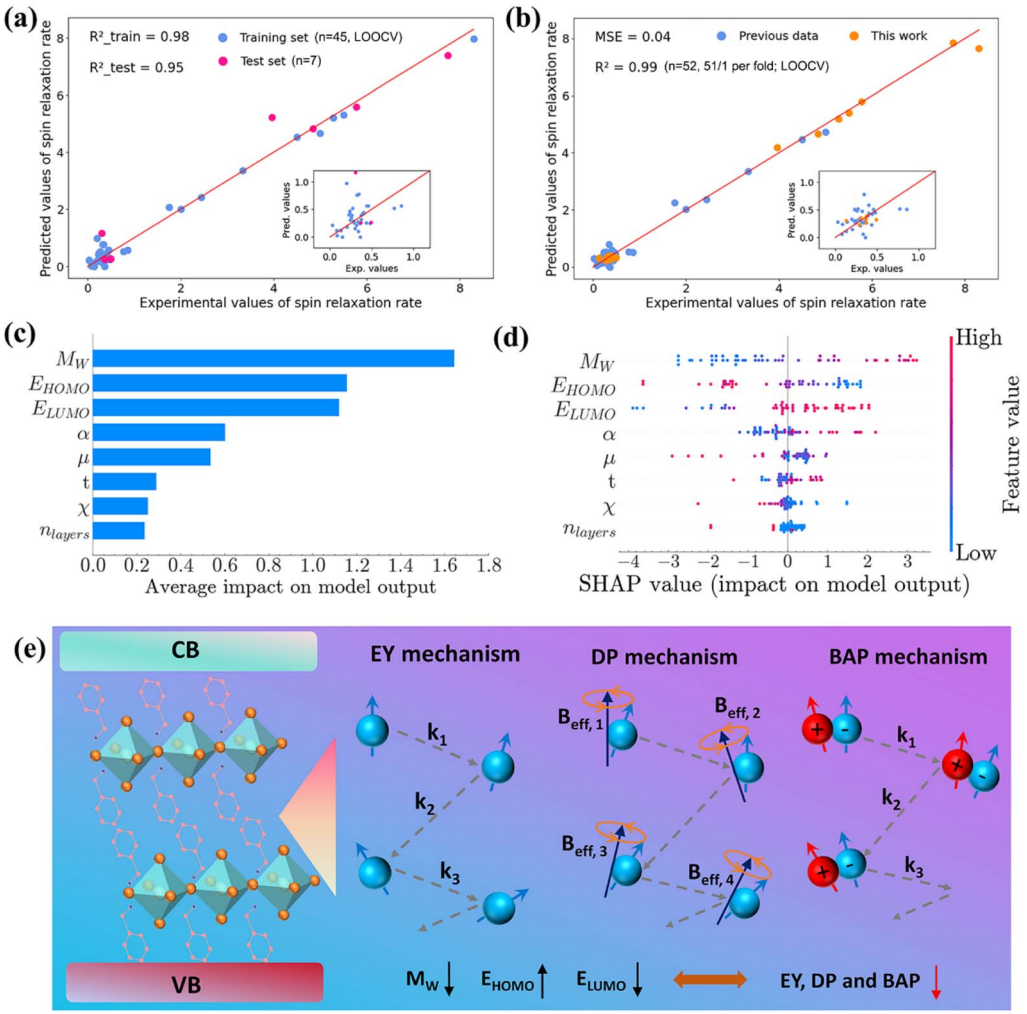

Fig. 5 (a) Predictive performance of the ANN model trained on 45 samples (38 literature + 7 synthesized) and evaluated on 7 unseen synthesized perovskite compounds. Blue dots denote training samples and magenta dots denote independent test samples; the red line indicates $y = x$. The training-set R^2 shown here is computed by LOOCV on the 45-sample training subset, whereas the test-set R^2 is computed on the independent 7-sample test set. The inset highlights the low-value region (spin-relaxation rate < 1). (b) Parity plot comparing predicted and experimental spin-relaxation rates for the ANN model evaluated by LOOCV on the full dataset ($n = 52$). Blue dots represent 38 literature-derived samples, while orange dots correspond to 14 perovskite materials synthesized and ultrafast-characterized in this work. The R^2 reported in this panel corresponds to LOOCV over all 52 samples. The inset shows a magnified view of the low-rate region. (c) Mean SHAP values quantifying the relative importance of each feature. (d) SHAP summary plot illustrating the directionality and magnitude of each feature's contribution across all samples. (e) Schematic illustration of the physical mechanisms underlying spin relaxation in perovskite materials, including the EY, DP, and BAP mechanisms.

of 0.04. The training process converged after more than 1300 iterations, as detailed in Fig. S8. These results further confirm that the refined descriptor framework—composed entirely of intrinsic, fully computable physical parameters—can accurately model spin relaxation behaviour in perovskite materials without relying on any experimentally derived structural features, offering both strong predictive performance and physical interpretability. Table S7 lists the experimental and LOOCV-predicted spin relaxation rates for all 52 perovskite samples used in the final model evaluation.

In addition, the model's residual distribution supports its overall reliability and balance. The residuals followed a near-Gaussian unimodal profile with minimal outliers (see Fig. S9), indicating the absence of systematic bias across the response space. Notably, despite being constructed exclusively from intrinsic descriptors, the model maintained consistent performance across various perovskite compositions, demonstrating its compositional agnosticism and broad generalizability. These characteristics make the model highly promising for large-scale material screening and early-stage design of spin-functional perovskite systems.

To gain deeper insight into the contribution of each intrinsic descriptor to the model's predictions, we performed SHAP analysis on the ANN model trained using LOOCV on the full dataset. As shown in Fig. 5c and d, M_W, E_{HOMO}, and E_{LUMO} emerged as the most influential features, followed by α and μ, all exhibiting significantly higher mean SHAP values compared to the remaining descriptors. Moreover, the SHAP value distribution in

Fig. 5d further revealed the directionality of each feature's impact, illustrating how variations in individual descriptors influence the predicted spin relaxation rate. Based on an in-depth analysis of the SHAP interpretability results, we further examined how key intrinsic descriptors—namely M_W, E_{HOMO}, E_{LUMO}, α, and μ—influence spin relaxation mechanisms, and elucidated the underlying microscopic physical pathways. As shown in Fig. 5d, M_w exhibits the most pronounced directional contribution to the predicted spin relaxation rate, with samples possessing higher M_w predominantly appearing in the positive SHAP value region—indicating their unfavourable impact on spin lifetime extension. This effect is primarily ascribed to the fact that bulky organic cations often feature complex molecular geometries and significant steric hindrance, which can induce local lattice distortions and inversion symmetry breaking. These structural perturbations enhance Rashba-type spin–momentum coupling, thereby accelerating spin decoherence *via* the DP mechanism. Additionally, larger organic moieties tend to soften the lattice and lower phonon energies, which promotes stronger spin–phonon interactions and increases spin-flip events through the EY pathway. Furthermore, the presence of halogen atoms or highly polarizable functional groups in heavier cations may introduce internal electric field disturbances, further amplifying SOC and undermining spin coherence. Although M_w does not explicitly account for the heavy atoms intrinsic to the perovskite lattice (*e.g.*, Pb and I), its associated structural consequences exert a cascading influence across all three principal spin relaxation mechanisms.

A higher E_{HOMO} is closely associated with a prolonged spin lifetime. When the HOMO level increases, the valence band maximum shifts closer to the vacuum level, and the corresponding hole states exhibit greater delocalization. The expanded spatial distribution of the hole wavefunction reduces its overlap with electrons, thereby effectively weakening the exchange interactions that govern spin-flip events *via* the BAP mechanism. In two-dimensional perovskites, strong quantum confinement effects amplify the sensitivity of the band structure to changes in the HOMO level. The upward shift of the HOMO level leads to reduced valence band curvature and enhanced band degeneracy, which help suppress Rashba-type spin–momentum coupling, thus inhibiting spin decoherence *via* the DP mechanism. Furthermore, the elevated energy level may also reduce the energy resonance between hole states and phonons, consequently lowering the probability of spin–phonon scattering and diminishing the contribution of the EY mechanism. Likewise, a lower E_{LUMO} is also favourable for extending spin lifetime. A deeper conduction band minimum implies stronger electron binding and a higher degree of localization, which facilitates the formation of more stable bound excitons and significantly reduces the spatial overlap between electron and hole wavefunctions. This, in turn, suppresses spin-flip processes mediated by the BAP mechanism. In two-dimensional systems with pronounced quantum confinement, enhanced electron localization further limits interactions with lattice phonons, thereby weakening spin–phonon coupling and reducing the impact of the EY mechanism. In addition, a deeper LUMO level contributes to improved conduction band symmetry and enhanced degeneracy, which collectively mitigate Rashba spin splitting and suppress spin precession decoherence associated with the DP mechanism. This mechanistic interpretation is illustrated in Fig. 5e, which summarizes the dominant spin relaxation pathways and highlights how each key descriptor modulates the EY, DP, and BAP mechanisms through structural, electronic, and interfacial effects.

Within the hydrogenic/Wannier–Mott framework, E_b is primarily governed by the carrier reduced effective mass (m^*) and the dielectric constant (ε). The frontier orbital energies E_{HOMO} and E_{LUMO} (and their separation ΔE_{H-L}) strongly affect band alignment, effective carrier mass, and electron–hole wavefunction overlap, thereby indirectly modulating m^* and the exchange interaction strength, which in turn influence E_b. In contrast, molecular weight (M_w) is often correlated with the size, geometry, and polarizability of the organic cation, which modifies the dielectric environment and quantum confinement in layered perovskites, ultimately affecting the effective dielectric screening ε. Therefore, E_{HOMO}, E_{LUMO}, and M_w are intrinsically coupled to E_b through two key control parameters, m^* and ε. As a result, even without explicitly incorporating E_b into the model, our selected intrinsic descriptors effectively capture the core physical contributions of E_b to spin relaxation. This explains why the model successfully reproduces trends consistent with literature observations while maintaining a fully pre-synthetic and computation-accessible framework, clarifying the intrinsic connection between molecular weight (M_w), frontier orbital energies (E_{HOMO} and E_{LUMO}), and the exciton binding energy (E_b).

Although α and μ rank lower in the feature importance hierarchy, their mechanistic roles are well-defined and provide meaningful, supplementary insights into spin relaxation dynamics. Specifically, lower polarizability reflects increased electronic rigidity, which helps suppress interfacial charge fluctuations and mitigate Rashba spin splitting, thereby reducing spin decoherence *via* the DP mechanism. In parallel, reduced polarizability also diminishes the susceptibility of the organic cation to phonon-induced perturbations, weakening spin–phonon coupling and thus lowering the contributions from the EY mechanism. Moreover, a more stable electronic distribution may indirectly attenuate exchange interactions, further suppressing BAP-mediated spin relaxation.

Conversely, a higher μ enhances electrostatic coupling at the organic–inorganic interface, facilitating exciton delocalization and charge separation, which reduces electron–hole overlap and weakens the BAP pathway. Additionally, the tendency of high-dipole moment cations to adopt ordered orientations reduces conformational fluctuations and structural disorder, thereby limiting phonon-driven scattering channels associated with the EY mechanism. The preservation of local symmetry at the interface may also help suppress Rashba splitting, further mitigating DP-induced spin precession.

Taken together, these five descriptors—molecular weight, HOMO and LUMO energies, polarizability, and dipole moment—collectively regulate spin relaxation across structural, electronic, and interfacial dimensions, offering a comprehensive framework for understanding and engineering spin coherence in hybrid perovskite materials. Based on the

physically meaningful trends revealed by the SHAP analysis, we further leveraged the trained ANN model to perform exploratory screening of extended combinations of organic cations within the existing dataset. By prioritizing cation combinations featuring lower M_w, higher E_{HOMO}, lower E_{LUMO}, and reduced α, we predicted a potential material candidate, $(EOA)_2(FA)_3Pb_4I_{13}$, to exhibit an exceptionally low spin relaxation rate, with an estimated $1/\tau$ value of approximately 0.01 ps^{-1}. However, despite the promising prediction of a low spin relaxation rate for this material, its actual synthesis remains highly challenging. The primary difficulty lies in controlling crystal growth and retaining structural stability. Due to the strong polarity and hydrogen-bonding characteristics of EOA, it is difficult to distinguish and stabilize the $n = 4$ phase during solution growth, as $n = 3$ and $n = 5$ phases tend to coexist, leading to mixed-phase products and reduced phase purity. Additionally, the strong coordination between EOA and PbI_2 causes rapid nucleation and defect accumulation, making it difficult to obtain high-quality single crystals with flat terraces and smooth surfaces. To address these challenges, we will continue to optimize precursor chemistry, crystal growth kinetics, and environmental control conditions in future work, and explore more suitable solvent systems and temperature control methods in order to achieve reproducible synthesis of this material and experimentally validate the predicted long spin relaxation lifetime. Notably, this screening process was not conducted by optimizing a single descriptor independently, but rather was guided by the coordinated modulation of multiple intrinsic features consistent with physical intuition, further illustrating the model's potential utility for rational material selection and performance-driven design.

Conclusions

In this study, we developed a small-sample machine learning framework to enable accurate, pre-synthetic prediction of spin relaxation rates in perovskite materials. By combining 38 literature-reported samples with 14 experimentally synthesized and characterized compounds, we constructed an ANN model trained exclusively on intrinsic descriptors that are either quantum-chemically computable or composition-derived. The model achieved a high predictive accuracy ($R^2 = 0.99$) under LOOCV, following successful validation on an independent test set through a 45 + 7 split. SHAP-based interpretability analysis further revealed that molecular weight, HOMO energy, and LUMO energy are the dominant contributors to the model output, reflecting their key roles in modulating spin–orbit coupling, phonon scattering, and charge exchange dynamics. Polarizability and dipole moment also exhibited secondary contributions, further supporting the physical relevance of the selected features. Overall, this work provides a robust and interpretable prediction strategy that bridges machine learning and spin physics. It offers practical guidance for molecular-level design and high-throughput discovery of next-generation spin-functional perovskite materials.

Author contributions

Jianhui Li collected and curated the dataset, developed feature descriptors, conducted experimental testing, performed data analysis, and wrote the original draft of the manuscript. Xihan Chen conceived the project, collected data, supervised the study, contributed to descriptor design and data interpretation, and revised the manuscript. MingXi Chen developed and analyzed machine learning models and contributed to manuscript drafting. X. D. Xiang contributed to model optimization, supervised machine learning analysis, and revised the manuscript. Pan Wang and Lingling Mao synthesized and characterized the two-dimensional perovskite materials and assisted in experimental validation and data acquisition. Xiaohong Li and Kemi Ding assisted in machine learning model development, contributed to data analysis, and revised the manuscript. All authors discussed the results and contributed to the final version of the manuscript.

Conflicts of interest

There are no conflicts to declare.

Data availability

Machine learning code can be requested from the corresponding author at chenxh@sustech.edu.cn.

The data supporting this article have been included as part of the supplementary information (SI). Supplementary information: detailed machine learning procedure, synthesis procedures and reagents of 14 synthesized perovskite crystals, XRD and absorption data of synthesized crystals, transient spectra and transient kinetics of synthesized crystals, and predicted lifetime *vs.* measured lifetime. See DOI: **https://doi.org/10.1039/d5sc07406a**.

Acknowledgements

The study was supported by the National Natural Science Foundation of China with grant number 22103034 and 22275077. The study was also supported by Guangdong Major Project of Basic and Applied Basic Research (2023B0303000002).

Notes and references

1 S. Wolf, D. Awschalom, R. Buhrman, J. Daughton, v. S. von Molnár, M. Roukes, A. Y. Chtchelkanova and D. Treger, Spintronics: a spin-based electronics vision for the future, *Science*, 2001, **294**, 1488–1495.
2 D. Awschalom and D. Loss, *Semiconductor spintronics and quantum computation*, Springer Science & Business Media, 2002.
3 S. M. Yakout, Spintronics: future technology for new data storage and communication devices, *J. Supercond. Novel Magn.*, 2020, **33**, 2557–2580.
4 P. Dey and J. N. Roy, *Spintronics*, Springer, 2021.

5 M. A. Haque and M. C. Beard, Spin effects in metal halide perovskite semiconductors, *Nanoscale*, 2025, **17**, 9895–9906.
6 D. D. Awschalom and M. E. Flatté, Challenges for semiconductor spintronics, *Nat. Phys.*, 2007, **3**, 153–159.
7 H. Ohno, Toward functional spintronics, *Science*, 2001, **291**, 840–841.
8 J. Devkota, R. Geng, R. C. Subedi and T. D. Nguyen, Organic spin valves: a review, *Adv. Funct. Mater.*, 2016, **26**, 3881–3898.
9 L. Guo, S. Hu, X. Gu, R. Zhang, K. Wang, W. Yan and X. Sun, Emerging spintronic materials and functionalities, *Adv. Mater.*, 2024, **36**, 2301854.
10 J. Cardellino, N. Scozzaro, M. Herman, A. J. Berger, C. Zhang, K. C. Fong, C. Jayaprakash, D. V. Pelekhov and P. C. Hammel, The effect of spin transport on spin lifetime in nanoscale systems, *Nat. Nanotechnol.*, 2014, **9**, 343–347.
11 H. Lu, Z. V. Vardeny and M. C. Beard, Control of light, spin and charge with chiral metal halide semiconductors, *Nat. Rev. Chem.*, 2022, **6**, 470–485.
12 A. Privitera, M. Righetto, F. Cacialli and M. K. Riede, Perspectives of organic and perovskite-based spintronics, *Adv. Opt. Mater.*, 2021, **9**, 2100215.
13 T. Leijtens, G. E. Eperon, N. K. Noel, S. N. Habisreutinger, A. Petrozza and H. J. Snaith, Stability of metal halide perovskite solar cells, *Adv. Energy Mater.*, 2015, **5**, 1500963.
14 S. D. Stranks and H. J. Snaith, Metal-halide perovskites for photovoltaic and light-emitting devices, *Nat. Nanotechnol.*, 2015, **10**, 391–402.
15 H. P. Wang, S. Li, X. Liu, Z. Shi, X. Fang and J. H. He, Low-dimensional metal halide perovskite photodetectors, *Adv. Mater.*, 2021, **33**, 2003309.
16 J. Wang, C. Zhang, H. Liu, X. Liu, H. Guo, D. Sun and Z. V. Vardeny, Tunable spin characteristic properties in spin valve devices based on hybrid organic–inorganic perovskites, *Adv. Mater.*, 2019, **31**, 1904059.
17 I. Žutić, J. Fabian and S. D. Sarma, Spintronics: Fundamentals and applications, *Rev. Mod. Phys.*, 2004, **76**, 323.
18 W. Li, L. Zhou, O. V. Prezhdo and A. V. Akimov, Spin–orbit interactions greatly accelerate nonradiative dynamics in lead halide perovskites, *ACS Energy Lett.*, 2018, **3**, 2159–2166.
19 Y. Zhai, S. Baniya, C. Zhang, J. Li, P. Haney, C.-X. Sheng, E. Ehrenfreund and Z. V. Vardeny, Giant Rashba splitting in 2D organic-inorganic halide perovskites measured by transient spectroscopies, *Sci. Adv.*, 2017, **3**, e1700704.
20 X. Chen, H. Lu, K. Wang, Y. Zhai, V. Lunin, P. C. Sercel and M. C. Beard, Tuning spin-polarized lifetime in two-dimensional metal–halide perovskite through exciton binding energy, *J. Am. Chem. Soc.*, 2021, **143**, 19438–19445.
21 L. Zhang, J. Jiang, C. Multunas, C. Ming, Z. Chen, Y. Hu, Z. Lu, S. Pendse, R. Jia and M. Chandra, Room-temperature electrically switchable spin–valley coupling in a van der Waals ferroelectric halide perovskite with persistent spin helix, *Nat. Photonics*, 2022, **16**, 529–537.
22 Y. Huang, C. Chen, S. Gong, Q. Hu, J. Liu, H. Chen, L. Mao and X. Chen, Tuning spin-polarized lifetime at high carrier density through deformation potential in Dion–Jacobson-phase perovskites, *J. Am. Chem. Soc.*, 2024, **146**, 12225–12232.
23 Y. Huang, S. Gong, Q. Chen, C. Chen, Z. Yang, K. Wang, J. Xue, D. Wang, H. Lu, L. Mao, Y. Yang, J. Z. Zhao and X. Chen, Giant deformation potential induced small polaron effect in Dion–Jacobson two-dimensional lead halide perovskites, *Natl. Sci. Rev.*, 2025, **12**, nwae461.
24 H. Lu, J. Wang, C. Xiao, X. Pan, X. Chen, R. Brunecky, J. J. Berry, K. Zhu, M. C. Beard and Z. V. Vardeny, Spin-dependent charge transport through 2D chiral hybrid lead-iodide perovskites, *Sci. Adv.*, 2019, **5**, eaay0571.
25 Y.-H. Kim, Y. Zhai, H. Lu, X. Pan, C. Xiao, E. A. Gaulding, S. P. Harvey, J. J. Berry, Z. V. Vardeny and J. M. Luther, Chiral-induced spin selectivity enables a room-temperature spin light-emitting diode, *Science*, 2021, **371**, 1129–1133.
26 Y. Dong, M. P. Hautzinger, M. A. Haque and M. C. Beard, Chirality-Induced Spin Selectivity in Hybrid Organic-Inorganic Perovskite Semiconductors, *Annu. Rev. Phys. Chem.*, 2025, **76**, 519–537.
27 J. Kikkawa, I. Smorchkova, N. Samarth and D. Awschalom, Room-temperature spin memory in two-dimensional electron gases, *Science*, 1997, **277**, 1284–1287.
28 J. Kikkawa and D. Awschalom, Resonant spin amplification in n-type GaAs, *Phys. Rev. Lett.*, 1998, **80**, 4313.
29 N. Gedik and J. Orenstein, Absolute phase measurement in heterodyne detection of transient gratings, *Opt. Lett.*, 2004, **29**, 2109–2111.
30 M. Baranowski and P. Plochocka, Excitons in metal-halide perovskites, *Adv. Energy Mater.*, 2020, **10**, 1903659.
31 D. Pariari, S. Mehta, S. Mandal, A. Mahata, T. Pramanik, S. Kamilya, A. Vidhan, T. N. Guru Row, P. K. Santra and S. K. Sarkar, Realizing the lowest bandgap and exciton binding energy in a two-dimensional lead halide system, *J. Am. Chem. Soc.*, 2023, **145**, 15896–15905.
32 D. T. Ahneman, J. G. Estrada, S. Lin, S. D. Dreher and A. G. Doyle, Predicting reaction performance in C–N cross-coupling using machine learning, *Science*, 2018, **360**, 186–190.
33 T. Mou, H. S. Pillai, S. Wang, M. Wan, X. Han, N. M. Schweitzer, F. Che and H. Xin, Bridging the complexity gap in computational heterogeneous catalysis with machine learning, *Nat. Catal.*, 2023, **6**, 122–136.
34 P. M. Maffettone, L. Banko, P. Cui, Y. Lysogorskiy, M. A. Little, D. Olds, A. Ludwig and A. I. Cooper, Crystallography companion agent for high-throughput materials discovery, *Nat. Comput. Sci.*, 2021, **1**, 290–297.
35 E. Ozer, J. Kufel, J. Myers, J. Biggs, G. Brown, A. Rana, A. Sou, C. Ramsdale and S. White, A hardwired machine learning processing engine fabricated with submicron metal-oxide thin-film transistors on a flexible substrate, *Nat. Electron.*, 2020, **3**, 419–425.
36 K. Yazdani, D. Jordan, M. Yang, C. R. Fullenkamp, D. R. Calabrese, R. Boer, T. Hilimire, T. E. Allen, R. T. Khan and J. S. Schneekloth Jr, Machine learning informs RNA-binding chemical space, *Angew. Chem., Int. Ed.*, 2023, **135**, e202211358.

37 Z. Su, B. Dai, X. Wang, Y. Jiang, W. Lin and C. Wang, Machine Learning Reveals In-Cavity vs Surface Activity for Selective C–H Borylation by Metal-Organic Framework Catalysts, *Angew. Chem., Int. Ed.*, 2025, **64**, e202505931.

38 B. J. Shields, J. Stevens, J. Li, M. Parasram, F. Damani, J. I. M. Alvarado, J. M. Janey, R. P. Adams and A. G. Doyle, Bayesian reaction optimization as a tool for chemical synthesis, *Nature*, 2021, **590**, 89–96.

39 Y. Liu, K. P. Kelley, R. K. Vasudevan, H. Funakubo, M. A. Ziatdinov and S. V. Kalinin, Experimental discovery of structure–property relationships in ferroelectric materials via active learning, *Nat. Mach. Intell.*, 2022, **4**, 341–350.

40 A. Merchant, S. Batzner, S. S. Schoenholz, M. Aykol, G. Cheon and E. D. Cubuk, Scaling deep learning for materials discovery, *Nature*, 2023, **624**, 80–85.

41 H. Yang, J. Li, K. Z. Lim, C. Pan, T. Van Truong, Q. Wang, K. Li, S. Li, X. Xiao and M. Ding, Automatic strain sensor design via active learning and data augmentation for soft machines, *Nat. Mach. Intell.*, 2022, **4**, 84–94.

42 J. Wu, L. Torresi, M. Hu, P. Reiser, J. Zhang, J. S. Rocha-Ortiz, L. Wang, Z. Xie, K. Zhang and B.-w. Park, Inverse design workflow discovers hole-transport materials tailored for perovskite solar cells, *Science*, 2024, **386**, 1256–1264.

43 F. Lu, Y. Liang, N. Wang, L. Zhu and J. Wang, Machine learning for perovskite optoelectronics: a review, *Adv. Photonics*, 2024, **6**, 054001.

44 Z. Chen, J. Wang, C. Li, B. Liu, D. Luo, Y. Min, N. Fu and Q. Xue, Highly versatile and accurate machine learning methods for predicting perovskite properties, *J. Mater. Chem. C*, 2024, **12**, 15444–15453.

45 X. Chen, H. Lu, Z. Li, Y. Zhai, P. F. Ndione, J. J. Berry, K. Zhu, Y. Yang and M. C. Beard, Impact of layer thickness on the charge carrier and spin coherence lifetime in two-dimensional layered perovskite single crystals, *ACS Energy Lett.*, 2018, **3**, 2273–2279.

46 M. A. Kempf, P. Moser, M. Tomoscheit, J. Schröer, J.-C. Blancon, R. Schwartz, S. Deb, A. Mohite, A. V. Stier and J. J. Finley, Rapid spin depolarization in the layered 2d ruddlesden–popper perovskite (BA)(MA) PbI, *ACS Nano*, 2023, **17**, 25459–25467.

47 G. Yumoto, F. Sekiguchi, R. Hashimoto, T. Nakamura, A. Wakamiya and Y. Kanemitsu, Rapidly expanding spin-polarized exciton halo in a two-dimensional halide perovskite at room temperature, *Sci. Adv.*, 2022, **8**, eabp8135.

48 S. B. Todd, D. B. Riley, A. Binai-Motlagh, C. Clegg, A. Ramachandran, S. A. March, J. M. Hoffman, I. G. Hill, C. C. Stoumpos and M. G. Kanatzidis, Detection of Rashba spin splitting in 2D organic-inorganic perovskite via precessional carrier spin relaxation, *APL Mater.*, 2019, **7**, 081116.

49 H. Zhou, Q. Feng, C. Sun, Y. Li, W. Tao, W. Tang, L. Li, E. Shi, G. Nan and H. Zhu, Robust excitonic light emission in 2D tin halide perovskites by weak excited state polaronic effect, *Nat. Commun.*, 2024, **15**, 8541.

50 S. A. Bourelle, R. Shivanna, F. V. Camargo, S. Ghosh, A. J. Gillett, S. P. Senanayak, S. Feldmann, L. Eyre, A. Ashoka and T. W. van de Goor, How exciton interactions control spin-depolarization in layered hybrid perovskites, *Nano Lett.*, 2020, **20**, 5678–5685.

51 S. A. Bourelle, F. V. Camargo, S. Ghosh, T. Neumann, T. W. van de Goor, R. Shivanna, T. Winkler, G. Cerullo and F. Deschler, Optical control of exciton spin dynamics in layered metal halide perovskites via polaronic state formation, *Nat. Commun.*, 2022, **13**, 3320.

52 Y. Zhang, B. Zhang, J. Wang, Y. Fu, Y. Han, J. Guo and X. Zhang, Spin Preserved Exciton Funneling through a Polaronic Intermediate State in Layered Perovskite Single Crystals, *Adv. Opt. Mater.*, 2023, **11**, 2202444.

53 P. Odenthal, W. Talmadge, N. Gundlach, R. Wang, C. Zhang, D. Sun, Z.-G. Yu, Z. Valy Vardeny and Y. S. Li, Spin-polarized exciton quantum beating in hybrid organic–inorganic perovskites, *Nat. Phys.*, 2017, **13**, 894–899.

54 A. K. Poonia, M. Shrivastava, W. J. Mir, J. Aneesh, A. Nag and K. Adarsh, Intervalley polaronic biexcitons in metal halide perovskite quantum dots, *Phys. Rev. B*, 2021, **104**, L161407.

55 W. Zhao, R. Su, Y. Huang, J. Wu, C. F. Fong, J. Feng and Q. Xiong, Transient circular dichroism and exciton spin dynamics in all-inorganic halide perovskites, *Nat. Commun.*, 2020, **11**, 5665.

56 S. Strohmair, A. Dey, Y. Tong, L. Polavarapu, B. J. Bohn and J. Feldmann, Spin polarization dynamics of free charge carriers in $CsPbI_3$ nanocrystals, *Nano Lett.*, 2020, **20**, 4724–4730.

57 M. Shrivastava, M. I. Bodnarchuk, A. Hazarika, J. M. Luther, M. C. Beard, M. V. Kovalenko and K. Adarsh, Polaron and spin dynamics in organic–inorganic lead halide perovskite nanocrystals, *Adv. Opt. Mater.*, 2020, **8**, 2001016.

58 M. Zhou, J. S. Sarmiento, C. Fei, X. Zhang and H. Wang, Effect of composition on the spin relaxation of lead halide perovskites, *J. Phys. Chem. Lett.*, 2020, **11**, 1502–1507.

59 J. Xue, Y. Huang, Y. Liu, Z. Chen, H. H. Y. Sung, I. D. Williams, Z. Zhu, L. Mao, X. Chen and H. Lu, Rashba Band Splitting and Bulk Photovoltaic Effect Induced by Halogen Bonds in Hybrid Layered Perovskites, *Angew. Chem., Int. Ed.*, 2023, **135**, e202304486.

60 H. Lei, Y. Xu, Y. Zhang, Q. Feng, H. Zhou, W. Tang, J. Wang, L. Li, G. Nan and W. Xu, Persistent Exciton Dressed by Weak Polaronic Effect in Rigid and Harmonic Lattice Dion–Jacobson 2D Perovskites, *ACS Nano*, 2024, **18**, 31485–31494.

61 S. Xu, Z. Chen, M. Qin, B. Cai, W. Li, R. Zhu, C. Xu and X.-D. Xiang, Developing new electrocatalysts for oxygen evolution reaction via high throughput experiments and artificial intelligence, *npj Comput. Mater.*, 2024, **10**, 194.

62 S. Xu, P. Chen, M. Qin, K. Jin and X. Xiang, Predicting superconducting temperatures with new hierarchical neural network AI model, *Front. Phys.*, 2025, **20**, 014205.

63 I. Jebli, F.-Z. Belouadha, M. I. Kabbaj and A. Tilioua, Prediction of solar energy guided by pearson correlation using machine learning, *Energy*, 2021, **224**, 120109.